Controls on water storage and drainage in crevasses on the Greenland Ice Sheet

T. R. Chudley[1]*, P. Christoffersen[1], S. H. Doyle[2], T. P. F. Dowling[3]†, R. Law[1], C. M. Schoonman[1]‡, M. Bougamont[1], and B. Hubbard[2]

[1] Scott Polar Research Institute, University of Cambridge

[2] Centre for Glaciology, Department of Geography and Earth Sciences, Aberystwyth University

[3] Department of Geography, King's College London

* Corresponding author: Tom Chudley (trc33@cam.ac.uk)

† Now at the National Centre for Earth Observation, Department of Physics & Astronomy, University of Leicester, University Road, Leicester, LE1 7RH, United Kingdom.

‡ Now at the Alfred Wegener Institute Helmholtz Centre for Polar and Marine Research, Bremerhaven, Germany.

Key Points:

- At a marine-terminating sector of the Greenland Ice Sheet, 26% of all crevasses ponded between 2017-2019; the rest remained unfilled.
- Ponded crevasse locations are persistent between years but, unlike supraglacial lakes, this distribution is not topographically controlled.
- Ponds occur under compressive stress regimes, likely due to hydraulic isolation by creep closure, and drain predominantly via hydrofracture.

Abstract

Surface crevasses on the Greenland Ice Sheet capture nearly half of the seasonal runoff, yet their role in transferring meltwater to the bed has received little attention compared to that of supraglacial lakes and moulins. Here, we present observations of crevasse ponding and investigate controls on their hydrological behaviour at a fast-moving, marine-terminating sector of the Greenland Ice Sheet. We map surface meltwater, crevasses, and surface-parallel stress across a ~2,700 km^2 region using satellite data and contemporaneous uncrewed aerial vehicle (UAV) surveys. From 2017-2019 an average of 26% of the crevassed area exhibited ponding at locations that remained persistent between years despite rapid advection rates. We find that the spatial distribution of ponded crevasses does not relate to previously proposed methods for predicting the distribution of supraglacial lakes (elevation and topography) or crevasses (von Mises stress thresholds), suggesting the operation of some other physical control(s). Ponded crevasse fields were preferentially located in regions of compressive surface-parallel mean stress, which we interpret to result from the hydraulic isolation of these systems, in contrast to unponded crevasse fields, which we suggest are able to drain into the wider supraglacial and englacial network. UAV observations show that ponded crevasses can drain episodically and rapidly, likely through hydrofracture. We therefore propose that the surface stress regime informs a spatially heterogeneous transfer of meltwater through crevasses to the bed of ice sheets, with potential consequences for processes such as subglacial drainage and the heating of ice via latent heat release by refreezing meltwater.

1 Introduction

Surface crevasses are open fractures in glaciers and ice sheets ranging in width from millimetres to tens of metres and in length from tens of metres to kilometres. Crevasses are a visible expression of a glacier's surface stress regimes; the size and orientation of crevasses are intrinsic to glacier dynamics as they are formed by extensional flow and deformation of ice through compression or shear (Colgan *et al.,* 2016). Studying crevasses provides insight into glacier flow (Phillips *et al.,* 2013; Dell *et al.,* 2019) and is important for the development of fracturing criteria for supraglacial lake drainage (Das *et al.,* 2008; Arnold *et al.,* 2014, Poinar and Andrews, 2021), ice calving (Benn *et al.,* 2017; Todd *et al.,* 2019), and for quantifying the dynamic influence of water transmitted to the bed of glaciers (McGrath *et al.,* 2011; Koziol & Arnold, 2018).

Crevasses are an important pathway for the transfer of water to the subglacial environment of glaciers and ice sheets, while water itself can drive the propagation of crevasses via hydrofracture (Weertman, 1973; Alley *et al.,* 2005; van der Veen, 2007; Krawczynski *et al.,* 2009). Once full-depth hydrofracture has occurred, water flow forms an efficient route for continued meltwater delivery to the bed in the form of moulins. Many studies of the Greenland Ice Sheet (GrIS) have largely focussed on supraglacial lake drainage as the primary method of routing surface meltwater to the ice sheet bed (Banwell *et al.,* 2016; Hoffman *et al.,* 2018; Christoffersen *et al.,* 2018). However, supraglacial lakes deliver less total meltwater volume to the ice sheet bed than crevasse fields, which may capture as much as half of seasonal surface runoff (McGrath *et al.,* 2011; Koziol *et al.,* 2017). The limited available studies of crevasse field hydrology that exist describe variable, sometimes mutually contradictory, drainage processes. Some studies observe discrete drainage of crevasses (Lampkin *et al.,* 2013; Cavanagh *et al.,* 2017), which appear to result from episodic full-depth hydrofracture and display parallels to supraglacial lake drainage events. In contrast, other studies suggest crevasse fields continuously,

but inefficiently, transmit a low water flux to the subglacial system without the need for full-depth hydrofracture (Colgan *et al.,* 2011; McGrath *et al.,* 2011). So far, no studies account for the full spectrum of observations and assumptions surrounding the routing of water through crevasse fields.

Furthermore, in parallel to this paucity of observational studies, crevasse field hydrology has predominantly been neglected in numerical models of GrIS surface hydrology (e.g. Arnold *et al.,* 2014; Banwell *et al.,* 2013, 2016), included in only the most recent studies (e.g. Clason *et al.,* 2015; Koziol *et al.,* 2017; Koziol & Arnold, 2018). Where crevasse hydrology is included, its presence is predicted using spatially homogeneous stress thresholds. The use of simple stress thresholds to predict hydrological behaviour is common across studies of GrIS supraglacial hydrology (Poinar *et al.,* 2015; Clason *et al.,* 2015; Everett *et al.,* 2016; Koziol *et al.,* 2017; Williamson, *et al.,* 2018). However, these thresholds are identified from observational studies performed with the purpose of identifying suitable predictors of crevasse presence, not crevasse hydrology (Vaughan, 1993; Hambrey & Müller, 1978; Harper *et al.,* 1998; van der Veen, 1998) - and may not even be suitable for that purpose (Mottram and Benn, 2009), as ice fracture is increasingly understood to be complex and multi-dimensional (van der Veen, 1999; Colgan *et al.,* 2016, Hubbard *et al.,* in press). To date, no observational studies exist to support the use of any such controls, stress or otherwise, on the hydrological behaviour of crevasses.

Here, we aim to use remote sensing to identify the diversity in, and controls on, the hydrological behaviour of crevasses on an ice sheet. We make use of large-scale, satellite-derived data to investigate the spatial variation of crevasse hydrological state across a ~2,700 km^2 sector of the GrIS between 2017 and 2019. Using this data, we identify the spatial heterogeneity in crevasse hydrological behaviour; the interannual variability of crevasse fields; and we test potential topographic and dynamic controls on such behaviour. We supplement these regional observations using repeat surveys of a ~7 km^2 sector of a fast-flowing crevasse field from an uncrewed aerial vehicle (UAV). These high spatial and temporal resolution observations allow for the identification of filling and drainage processes occurring at the scale of individual crevasses, as well as the validation of satellite observations.

2 Methods

2.1 Study Area

Our study area is a ~3000 km^2 sector of the western GrIS (Figure 1), which comprises six marine-terminating outlets extending from Sermeq Kujalleq (also known as Store Glacier; 70.4˚N 50.6˚W) in the south to Perlerfiup Sermia (71.0˚N, -50.9˚W) in the north. Within this large-scale region of interest (hereafter the 'satellite ROI'), we used UAV surveys and Structure-from-Motion with Multi-View Stereo (SfM-MVS) photogrammetry to assess, at high resolution, a crevasse field in the Store Glacier drainage basin, 25 km from the calving front (hereafter the 'UAV ROI'). The UAV ROI is 1.5 km wide and 5 km long, and was chosen based on its coverage of an initiating crevasse field, ranging from areas with no visible crevasses through to areas where crevasse width exceeds 50 m.

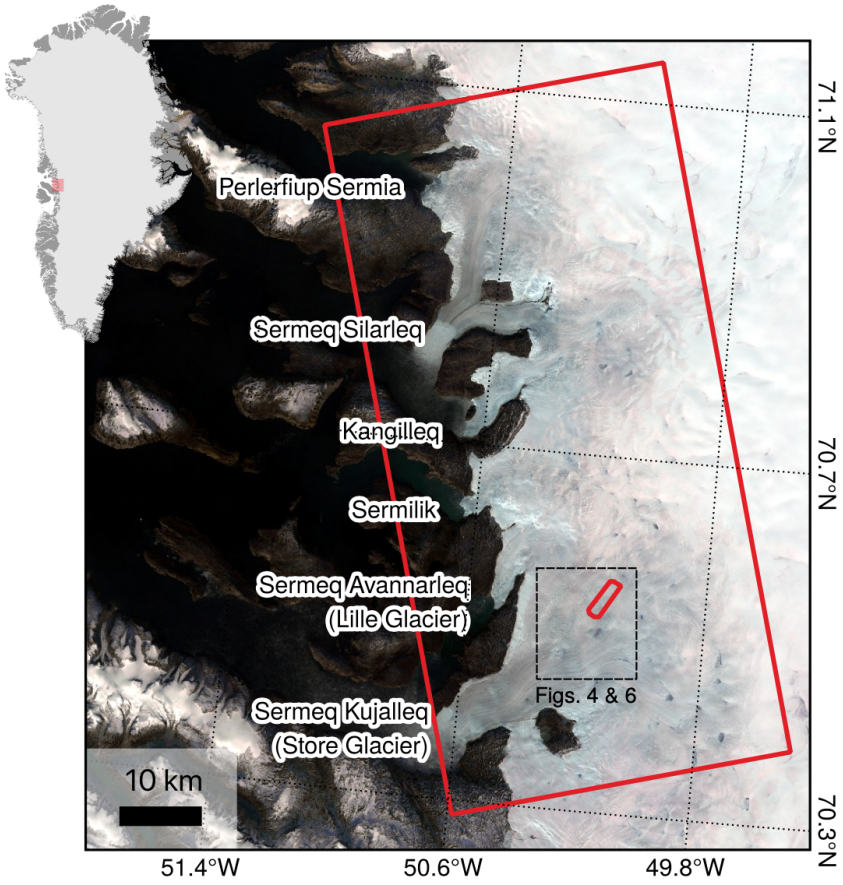

Figure 1. Map of study region. Small red box outlines the extent of UAV surveys. Large red box outlines the extent of satellite image analysis. Dotted line marks the extent of Figures 4 and 6. Marine-terminating outlet glaciers are labelled, with the alternative names in brackets where applicable. Background is a composite of median Sentinel-2 RGB pixel values between May-October 2018.

2.2 Satellite data

2.2.1 Crevasse classification

Crevasse identification from digital elevation models can be approached in a variety of ways (Florinsky & Bliakharskii, 2019), but we use a simple method that identifies crevasses from the residuals between the original and a smoothed digital elevation model (DEM). We output a binary crevasse mask of the satellite ROI using ArcticDEM v3 mosaic data at 2 m resolution (Porter *et al.,* 2018), processing the data in Google Earth Engine (Figure S1; Gorelick *et al.,* 2017) to allow for efficient computation over the ~2,700 km^2 study area. We first cropped the ArcticDEM to the GIMP ice mask (Howat *et al.,* 2014), before smoothing the elevation model by performing an image convolution with a circular kernel of 50 m radius. Residuals greater than 1 m between the smoothed and raw elevation values were identified as crevasses. To compare with glaciological stress estimates, the 2 m dataset was aggregated into grid cells to match the resolution (200 m) and projection (NSIDC sea ice polar stereographic north) of the MEaSUREs (Making Earth System Data Records for Use in Research Environments) 2018 ice sheet surface velocity grid. Aggregated values represent the fraction of grid cell area classified as crevasses. When partitioning into crevassed and non-crevassed regions of the ice sheet, we define a

126 'crevassed' pixel as that with >1% crevasse coverage. This low threshold value was chosen to
127 ensure that grid cells were still classified even where crevasses were small (e.g. upstream
128 crevasse fields), whilst still - based upon visual inspection - being sufficient to filter out grid
129 cells with false positive pixels.

130 We also classified crevasse initiation zones by manually locating the upstream boundary between
131 crevasse fields and bare ice from the 2 m crevasse dataset. The flow direction was determined
132 from 2018 MEaSUREs (Making Earth System Data Records for Use in Research Environments)
133 velocity data and a 200 m buffer around the linear boundary was used to identify pixels in the
134 dataset that should be classified as being in crevasse initiation zones.

135 *2.2.2 Water classification*

136 We produced a single binary map of water presence across the satellite ROI through the 2017-
137 2019 melt seasons using Sentinel-2 imagery in Google Earth Engine (Figure S2). These seasons
138 were selected based on the availability of Sentinel-2 data, with 2018 specifically selected to
139 match the timing of the UAV surveys on Store Glacier. We first identified all Sentinel-2 scenes
140 with <40% cloud cover and <70˚ solar zenith angle from May-October of each year. We clipped
141 the images to the GIMP ice mask (Howat *et al.,* 2014) and converted digital number values to
142 top of atmosphere reflectance. The latter have been shown to be suitable for identifying surface
143 water in Greenland from medium-resolution optical imagery (Pope, 2016), and have been used
144 for surface water classification in Sentinel-2 data (Williamson *et al.,* 2018a). We then calculated
145 the normalised difference water index (NDWI) from bands 2 (blue) and 4 (red) for all images.
146 Following Williamson *et al.* (2018a)'s parameterisation for the Store Glacier region (falling
147 within the satellite ROI), we used an NDWI threshold of 0.25 to create binary water
148 classification maps for each Sentinel-2 image. In order to avoid false positive identification of
149 shaded regions, we masked areas in topographic shadow, using the ArcticDEM (resampled to
150 Sentinel-2 resolution and projection) for topography and the solar zenith angle from Sentinel-2
151 image metadata. Finally, we summed the image stack to count the number of times through the
152 2018 melt season that a pixel was identified as water. To reduce false positive classifications
153 (e.g. cloud shadow, ephemeral slush zones at the beginning of the melt season) we classify as
154 water any pixel that was identified as water in ≥2 images through the melt season. As for
155 crevasse maps, we aggregate this data onto the velocity grid with a unit of fractional coverage of
156 water within each grid cell. When partitioning the ice sheet surface into 'ponded' and 'dry'
157 regions, we define a ponded pixel as that with >1% water coverage (following our 1% threshold
158 for crevassed pixels), and furthermore a 'lake-filled' pixel as that with >95% water coverage.
159 The latter value was selected as an appropriate classification threshold for lakes by comparing a
160 range of thresholds against the high-resolution annual water-presence maps.

161 *2.2.3 Topographic Analysis*

162 In order to explore the extent of topographic controls on crevasse surface hydrology, we
163 identified topographic sinks that would capture the surface flow of water by filling closed
164 depressions in the ice sheet surface, similar to previous studies of potential lake sites elsewhere
165 on the Greenland Ice Sheet (Ignéczi *et al.,* 2016). Before filling, the ArcticDEM data were

resampled to the resolution and projection of the velocity data. This process removed false depressions at high spatial scales and allowed intercomparison with other data.

2.2.4 Stress Analysis

Strain rate and stress thresholds are commonly used to predict crevasse formation and supraglacial lake drainage from estimates of surface velocity (e.g. Poinar *et al.,* 2015; Stevens *et al.,* 2015; Christoffersen *et al.,* 2018). Inferring stress from velocity-derived strain rate requires an additional estimate or assumption of ice temperature, but allows for comparability of critical failure thresholds between ice masses of varying temperature (Vaughan, 1993; Colgan *et al.,* 2016). We calculate simple stress thresholds previously proposed to control surface water routing in lake drainage studies, and assess their applicability to crevasse ponding. Specifically, we estimated the stress in the first and second principal directions (as applied by Poinar *et al.,* 2015 and Williamson, *et al.,* 2018), as well as the von Mises yield criterion (as applied by Clason *et al.,* 2015; Everett *et al.,* 2016; Koziol *et al.,* 2017; and Williamson *et al.,* 2018b), using Glen's flow law as the constitutive equation linking ice stress and strain rate. As a proxy for whether the dominant stress regime is extensional or compressive, we further calculated the mean surface-parallel stress from the first and second principal stresses.

Surface strain rates were derived from MEaSUREs gridded GrIS annual velocity data for 2018 (Joughin *et al.,* 2010), with extensional strain rates defined as positive. The surface strain rate tensor $\dot{\varepsilon}_{ij}$ is calculated from the surface-parallel components of velocity, *u* and *v* (in NSIDC Polar Stereographic North grid directions *x* and *y*), as

$$\dot{\epsilon}_{ij} = \begin{bmatrix} \frac{\partial u}{\partial x} & \frac{1}{2}\left(\frac{\partial v}{\partial x} + \frac{\partial u}{\partial y}\right) \\ \frac{1}{2}\left(\frac{\partial v}{\partial x} + \frac{\partial u}{\partial y}\right) & \frac{\partial v}{\partial y} \end{bmatrix} = \begin{bmatrix} \dot{\epsilon}_{xx} & \dot{\epsilon}_{xy} \\ \dot{\epsilon}_{xy} & \dot{\epsilon}_{yy} \end{bmatrix}. \quad (1)$$

Derivatives were approximated using the finite difference of the MEaSUREs velocity field. The stress tensor, σ_{ij}, was calculated following the Nye-Glen isotropic flow law (Glen, 1955; Nye, 1957) as

$$\sigma_{ij} = B\dot{\epsilon}_e^{(1-n)/n}\dot{\epsilon}_{ij}, \quad (2)$$

where *n* is the flow law exponent with value 3 and *B* is a viscosity parameter, which we assign a value of 324 kPa $a^{1/3}$ (Cuffey and Paterson, 2010) based on an assumed 10 m ice temperature of -5˚C. This uniform temperature assumption follows that made in other regional studies examining similar spatial scales (Clason *et al.,* 2015; Koziol *et al.,* 2017; Williamson *et al.,* 2018b), and matches observations made using distributed temperature sensing measurements at Store Glacier (Law *et al.,* in press). The effective strain rate, $\dot{\varepsilon}_e$, was then calculated following Cuffey and Paterson (2010) as

$$\dot{\epsilon}_e = \sqrt{\frac{1}{2}[\dot{\epsilon}_{xx}^2 + \dot{\epsilon}_{yy}^2] + \dot{\epsilon}_{xy}^2}. \quad (3)$$

Because only surface-parallel stresses are considered, σ_{ij} can be expressed by two principal stresses. The first surface-parallel principal stress, σ_1, was calculated as the highest (most extensional) eigenvalue of the stress tensor, and second surface-parallel principal stress, σ_2, as the lowest (most compressive) eigenvalue.

The von Mises stress, σ_V, was calculated from the surface-parallel principal stresses following Vaughan (1993) as

$$\sigma_v = \sqrt{\sigma_1^2 + \sigma_2^2 - \sigma_1\sigma_2} \quad . \tag{4}$$

A von Mises failure envelope was prescribed as the 95th percentile of the von Mises stress across the non-crevassed area, allowing up to 5% of the data to be misclassified (Vaughan, 1993).

The mean surface-parallel principal stress, σ_m, was calculated as the arithmetic mean of the first and second surface-parallel principal stresses as

$$\sigma_m = \frac{1}{2}[\sigma_1 + \sigma_2] \quad . \tag{5}$$

To explore the interaction between stress state and crevasse behaviour, we followed Vaughan (1993) in presenting data in the form of failure maps, presented in terms of the two surface-parallel principal stresses.

2.3 UAV data

2.3.1 UAV photogrammetry

We acquired aerial imagery over a 13-day period in July 2018 (Table S1) using a custom-built, fixed-wing UAV with 2.1 m wing span. Imagery was collected using a Sony α6000 24 MP camera with a fixed 16-mm lens, processed using Structure from-Motion with Multi-View Stereo (SfM-MVS) photogrammetry, and used to derive velocity fields within the UAV ROI as described by Chudley *et al.* (2019a). In brief, photogrammetry was performed using AgiSoft Metashape v.1.4.3 software, and geolocated by using an on-board L1 carrier-phase GPS unit (post- processed against a local on-ice ground station) to locate the position of aerial photos (Chudley *et al.,* 2019a). Outputs from the photogrammetric process were 0.15 m resolution orthophotos and 0.2 m resolution DEMs.

2.3.2 Surface classification

To date, UAV-based crevasse detection has been based on topographic analysis of DEMs (e.g. Ryan *et al.,* 2015; Florinsky & Bliakharskii, 2019). Although useful from a hazard assessment perspective (Florinsky & Bliakharskii, 2019), DEM-based methods alone cannot be used to identify features such as ponded or healed crevasses, while crevasse detection is also sensitive to threshold choice and ultimately DEM resolution (Jones *et al.,* 2018; Florinsky & Bliakharskii, 2019). To take advantage of the high spatial resolution and multi-dimensional outputs of UAV

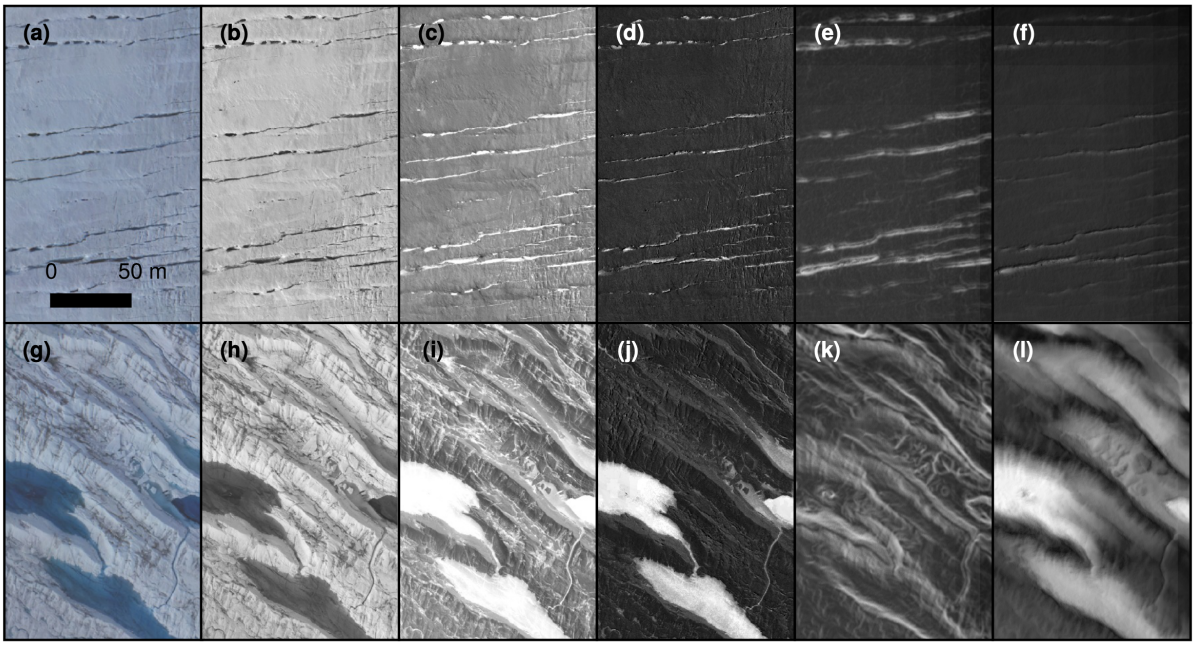

Figure 2. Examples of random forest input data for regions dominated by (a-f) small and (g-l) large crevasses. (a and g) RGB orthophotos. (b and h) Brightness. (c and i) Standard deviation of RGB values. (d and j) NDWI. (e and k) Slope, with hillshade overlaid. (f and l) Black-top-hat filtered DEM, with hillshade overlaid.

surveys, we used a combination of object-based image analysis (OBIA) and supervised classification to identify crevasses and their hydrological state in a survey of the UAV ROI flown on 2018-07-08. OBIA is based not on the numerical characteristics of individual pixels but on objects, i.e. groups of meaningfully similar pixels segmented according to spectral homogeneity (Blaschke, 2010). This has been used successfully in a glaciological context by Kraaijenbrink *et al.* (2016, 2018) for mapping cliff/pond systems and emissivity on a debris-covered glacier. We again used Google Earth Engine to perform the full segmentation and supervised classification workflow (Figure S2).

We identified a number of variables that could be used as inputs for a supervised classification algorithm to identify crevasse field surface features. This included: the red, green, and blue values of the orthophoto (Figure 2a;g); the 'brightness' (mean RGB values; Figure 2b;h) as per Kraaijenbrink *et al.* (2016); the standard deviation of the RGB values, which highlighted water, small crevasses, and healed crevasses (Figure 2c;i); the NDWI, from blue and red pixel values (Figure 2d;j); the DEM slope, which effectively highlighted small crevasses with widths on the order of a few metres (Figure 2e;k). Following Kodde *et al.* (2007), we also used DEM values that were black-top-hat filtered with a 30 m structuring element that was useful in identifying large crevasses with widths on the order of tens of metres (Figure 2f;l). A black top-hat filter morphologically closes the glacier surface at scales smaller than the structuring element, before subtracting the closed surface from the original data. This process was performed in MatLab prior to input into Google Earth Engine.

We performed image segmentation using Simple Non-Iterative Clustering (SNIC) (Achanta & Susstrunk, 2017), a computationally-efficient implementation of superpixel-based clustering. Rather than segmenting an image into semantically meaningful objects, superpixel-based segmentation aims to simplify the image into small, uniform, and compact clusters of similar pixels ('superpixels'), with a focus on boundary adherence. The variables described above were used as the input to the segmentation algorithm. We manually selected a seed spacing of 15 pixels (2.25 m) and a (relatively high) compactness factor of 200. This resulted in superpixels small enough to display strong boundary adherence to small and healed crevasses at the scale of metres, whilst still clearly delineating the margins of larger features such as water bodies. As an input to the supervised classification, we calculated the average and standard deviation of values in each superpixel from the variables described above, as well as the perimeter-to-area ratio of the superpixel, and normalised the results.

We adopted a supervised classification approach to surface classification (Kraaijenbrink *et al.,* 2016, 2018; Ryan *et al.,* 2018) by training a random forest classifier. Random forests make use of an ensemble of decision trees, which classify objects by applying a series of if-then-else logical conditions determined by training data. By utilising an ensemble of independent decision trees, random forests aim to avoid overfitting that may occur when using a single tree. Each tree utilises a randomised subset of training data, and the final result is gathered from a majority vote. To reduce the amount of redundant information used to train the classifier, we performed a non-parametric mutual information (MI) test on our training data as a proxy for the predictive power of each input variable. Rejecting input variables beneath the median MI value (Figure S3) did not noticeably reduce the accuracy of the output data (Figure S4). Therefore, we used only the nine most significant variables as inputs to the classifier. We constructed training datasets of 90 points each, distributed across the AOI, for six distinct surface types: bare ice, snow, healed crevasses, 'small' crevasses, 'large' crevasses, and water. We separated 'small' and 'large' crevasses (those with widths of metres vs. tens of metres) into two training datasets as they displayed distinctly different values for properties such as brightness, slope, and the top hat filtered DEM (Figure 2). We trained the classifier on two-thirds of the dataset (60 points per classification) and retained one-third (30 points per classification) for validation. Output classification performed well visually (Figure S5) and validation data showed that a >95% F_1 accuracy score was observed for all surface types (Figure S4, Table S2), apart from for snow and bare ice, which for our purposes were not important to distinguish. Although we identified six surface types, for this analysis we were only interested in three distinctions: crevasses (combining 'small' and 'large' crevasses), ice (combining bare ice, snow, and healed crevasses), and water.

3 Results

3.1 Satellite-based analysis

3.1.1 Ponded crevasse distribution

From the ArcticDEM elevation model and Sentinel-2 optical imagery, we mapped the distribution of crevasses (Figure 3a) and surface water (Figure 3b) across the study region. Of the total ice area assessed, ~34% (~960 km^2 out of ~2695 km^2) was classified as being crevassed (i.e. where a 200 m^2 grid cell has a crevasse fraction >1%). On average, 26% of this total crevassed region was observed to exhibit surface ponding (i.e. where a 200 m^2 grid cell has a

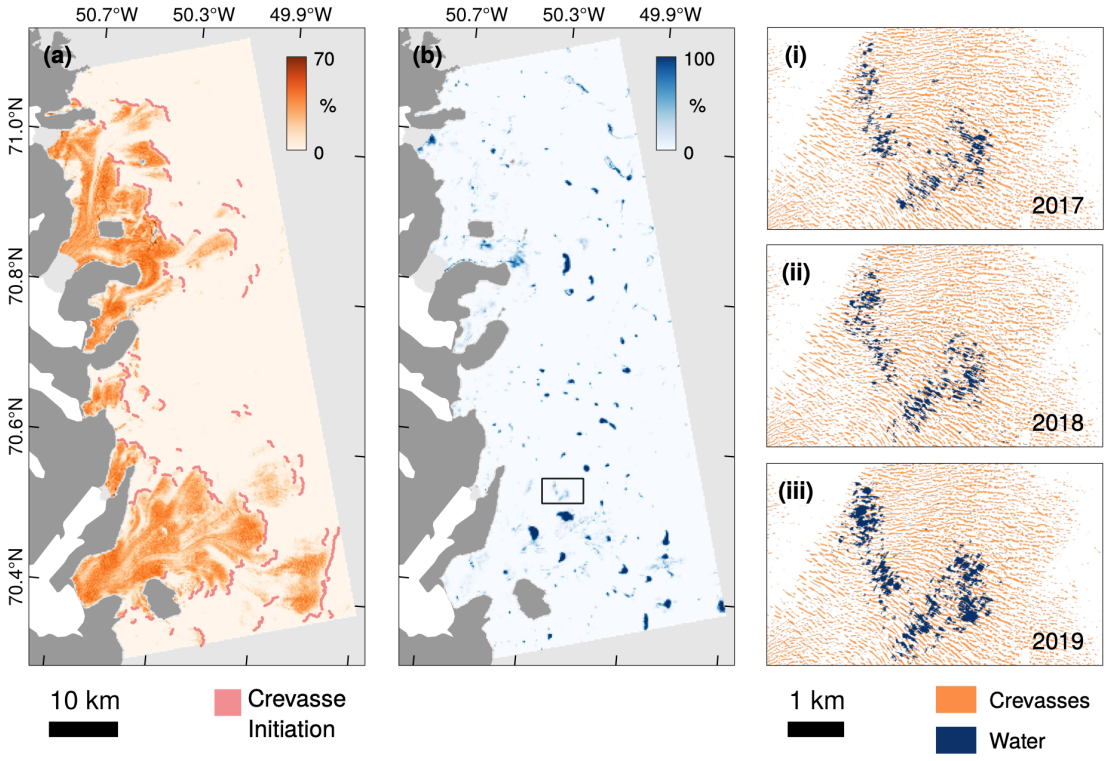

Figure 3. (a) Observed crevasse fraction at 200 m resolution derived from ArcticDEM data with 2 m resolution. Manually identified crevasse initiation zones are marked in red. (b) Mean 2017-2019 observed water fraction at 200 m resolution derived from Sentinel-2 data with 10 m resolution. Black box marks the extent of insets showing water presence (in blue) at Sentinel-2 base resolution (10 m) in (i) 2017; (ii) 2018; and (iii) 2019; and underlying crevasses (in orange) at the ArcticDEM base resolution (2 m).

Table 1. Crevassed area exhibiting surface ponding, by year.

Year	Crevassed area	Ponded crevassed area (absolute)	Ponded crevassed area (relative)
2017	960 km^2	190.2 km^2	19.8%
2018		264.9 km^2	27.6%
2019		290.0 km^2	30.2%
Mean		**235.4 km^2**	**24.5%**

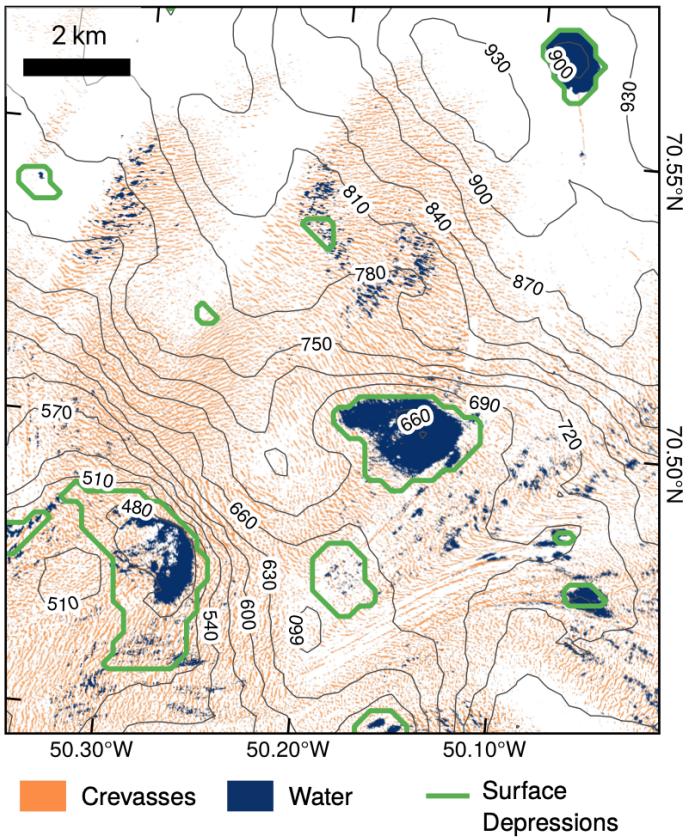

308

309 **Figure 4.** Boundaries of surface depressions (i.e. basins) overlaid onto Arctic-DEM derived crevasses and
310 2018 water extent. Contours, from ArcticDEM, are in height above ellipsoid in metres.
311

312 **Table 2.** Prevalence of surface types, classified according to ArcticDEM crevasse data and mean 2017-
313 2019 Sentinel-2 data, occurring within surface depressions.

Surface type	Grid cell classification thresholds	Proportion of surface type within depressions
Crevasse	>1% crevasse fraction	5.0%
Ponded crevasses (excluding lakes)	>1% crevasse fraction $1 < n <$ 95% water fraction	9.7%
Lake	>95% water fraction	78.9%

314

water fraction >1%) across the 2017-2019 ablation seasons, ranging from 20-30% (Table 1). Although total ponded area varies from year to year, the spatial pattern of ponded crevasses remained persistent between years. This can be observed qualitatively (Figure 3i-iii), and is supported by Pearson's correlation coefficient tests, which return statistically significant ($p < 0.01$) positive correlations when testing observed pixel water fraction between years (R^2 values: 2017-18, 0.68; 2018-19, 0.67; 2017-19, 0.79). The interannual spatial pattern of crevasse ponding is consistent across the study area despite ice velocity advecting crevasses kilometres per year in some areas, suggesting the ability of crevasses to pond is externally controlled rather than a property of individual crevasses.

3.1.2 Topographic analysis

If the ability of a crevasse to pond was solely dependent on meltwater availability, ponded crevasses would be more prevalent at lower elevations, where air temperature is higher. We tested this hypothesis by comparing the spatial distribution of satellite-derived water fraction (Figure 3b) with elevation. Within crevassed grid cells, there was no significant relationship between elevation and water fraction (R^2 value = 0.0014, $p < 0.01$). This analysis indicates that (air-temperature driven) meltwater availability does not exert a major control on ponded crevasse formation up to the limit of the elevation range of the satellite ROI (~1500 m a.s.l).

If crevasse systems pond due to receiving meltwater that has been transported laterally across supraglacial drainage networks, ponding should occur at the bottom of surface depressions. We tested this hypothesis by assessing the prevalence of meltwater ponding within surface depressions as identified from ArcticDEM data (Table 2). This analysis indicated that 78.9% of grid cells classified as lakes occurred in topographic depressions, whilst only 5.0% of crevassed grid cells and 9.7% of ponded crevasse grid cells were similarly located. Thus, while supraglacial lakes were predominantly located within surface basins (as expected), ponded crevasse fields were predominantly located outside such basins (Figure 4). Infilling of surface basins by lateral supraglacial water transport therefore appears to explain only a minority of crevasse ponding locations.

3.1.3 Stress analysis

We present strain-rate-derived stresses as failure maps, plotted in the form of density plots (Figure 5). To aid visualisation, each data point is plotted twice with assignments of σ_1 and σ_2 reversed, giving symmetry across the line $\sigma_1 = \sigma_2$. Based on the stress distribution of the non-crevassed area, the von Mises failure envelope was prescribed at 76 kPa (marked with ellipses in Figure 5). However, this threshold does not differentiate either crevasse incidence nor hydrological status. Crevasses plot both inside and outside the von Mises failure envelope (Figure 5b), while initiating crevasses (Figure 5c) plot predominantly within the envelope. The von Mises failure envelope is also not useful for differentiating crevasse ponding (Figure 5d). Inspection of Figure 5 does, however, reveal that initiating crevasses (Figure 5c) and ponding crevasses (Figure 5d) are separated by the line defined by $\sigma_1=-\sigma_2$ (dashed line in Figure 5). This line marks the transition in mean surface-parallel stress state (σ_m) from negative (compressional; below the line) to positive (extensional; above the line). Thus, this analysis reveals that 89% of initiating crevasses are located in areas of extensional stress (cf. 54% of all crevasses). In contrast, 68% of ponded crevasses are located within areas of compressive stress (cf. 46% of all

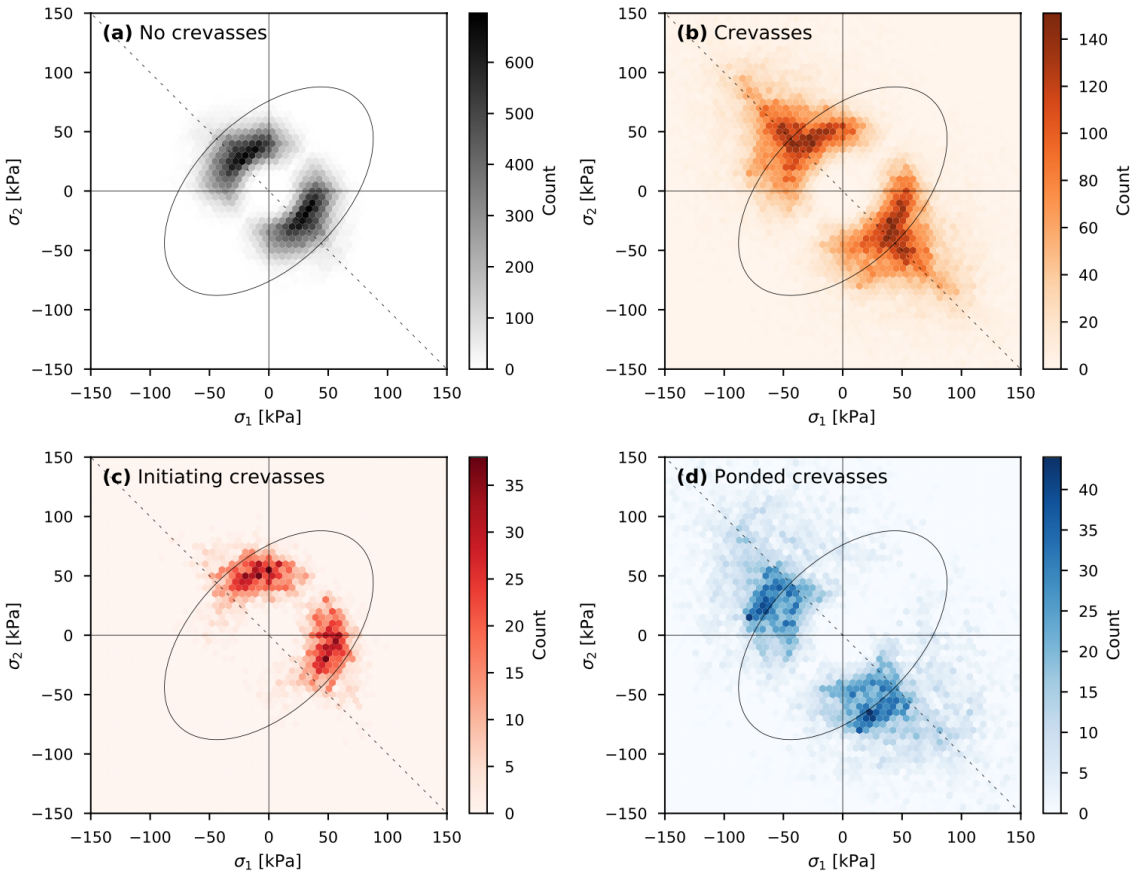

Figure 5. Failure maps in the form of density plots of surface-parallel stress states for selected surface classifications: (a) no crevasses; (b) all crevasses; (c) initiating crevasses; (d) water-filled crevasses. Ellipses mark the prescribed von Mises stress threshold (76 kPa). Dotted line marks where mean surface-parallel principal stress is zero. Note that data are reflected across the line X=Y.

crevasses). An example of the contrasting relationships between crevasse status and mean surface-parallel stress are plotted spatially in Figure 6. While not all crevasses that are located in compressive regimes pond, the transition between extensional and compressive σ_m regimes represents a convincing boundary between regions of crevasse initiation and ponding. This suggests that a compressive mean stress regime is a necessary, but not sufficient, condition of ponding.

3.2 UAV-based image analysis

UAV-derived observations of crevasse initiation and ponding (Figure 7a) follow similar patterns to those revealed by the regional-scale satellite data (Figure 7b). Crevasses initiated - or at least become identifiable in the decimetre-resolution data - in the upstream section of the study zone. As they are advected down-glacier, crevasses width increased from decimetres to a maximum of ~10–60 m (Figure 7a, i, ii). The region of crevasse initiation was coincident with a zone of extensional σ_m in the satellite-derived data (Figure 7b). In the downstream sector of the UAV ROI, crevasse size remained relatively stable, but displayed a higher propensity to pond in the

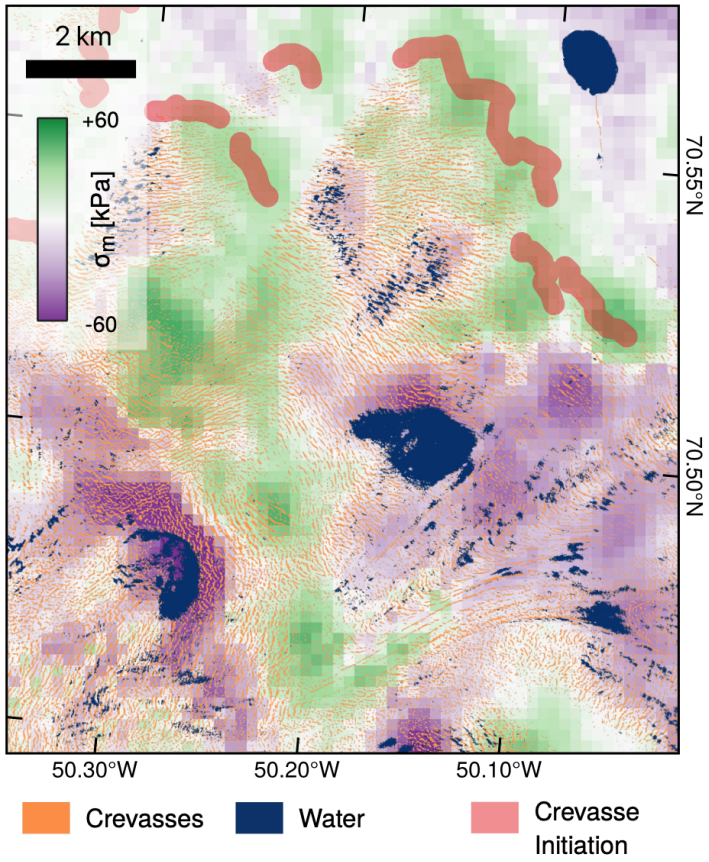

Figure 6. Crevasses, crevasse initiation zones, and 2018 water extent overlaid onto a shaded map of mean surface-parallel stress.

down-glacier direction (Figure 7a). This region of crevasse ponding occurs where satellite-derived σ_m is observed to be compressive (Figure 7b).

Repeat UAV surveys provide insight into processes occurring at the scale of individual crevasses. Over the 13-day period in July 2018 over which surveys were undertaken (Table S1), three crevasse systems in the UAV ROI were observed to drain, and six underwent significant filling. Crevasse drainages appear to be rapid. Of the three drainages identified, two represent crevasses that had a constant or rising water level in sequential imagery acquired prior to drainage. All three exhibited significant water loss between subsequent adjacent surveys (e.g. Figure 8a-b, c–d). One crevasse system lost a substantial volume of water in less than 24 hours (Figure 8a–b), and water levels continued to drop for the rest of the 12 day survey period (Figure S6b–c). This suggests that either a moulin had formed, and that water therefore continued to drain into the subglacial system, or that small open fractures continued to transfer water inefficiently into the englacial system. The filling crevasses were clustered tightly at the upstream side of the ponded crevasse system, in a location where crevasses are advecting from an extensional to compressive σ_m regime. Of the three crevasse drainage events identified, two occurred within the larger ponded system and compressive mean stress regime, while one occured in a smaller crevasse at the periphery of the system, in a weakly extensional regime. These observations are consistent with the satellite-based observations in that, in general,

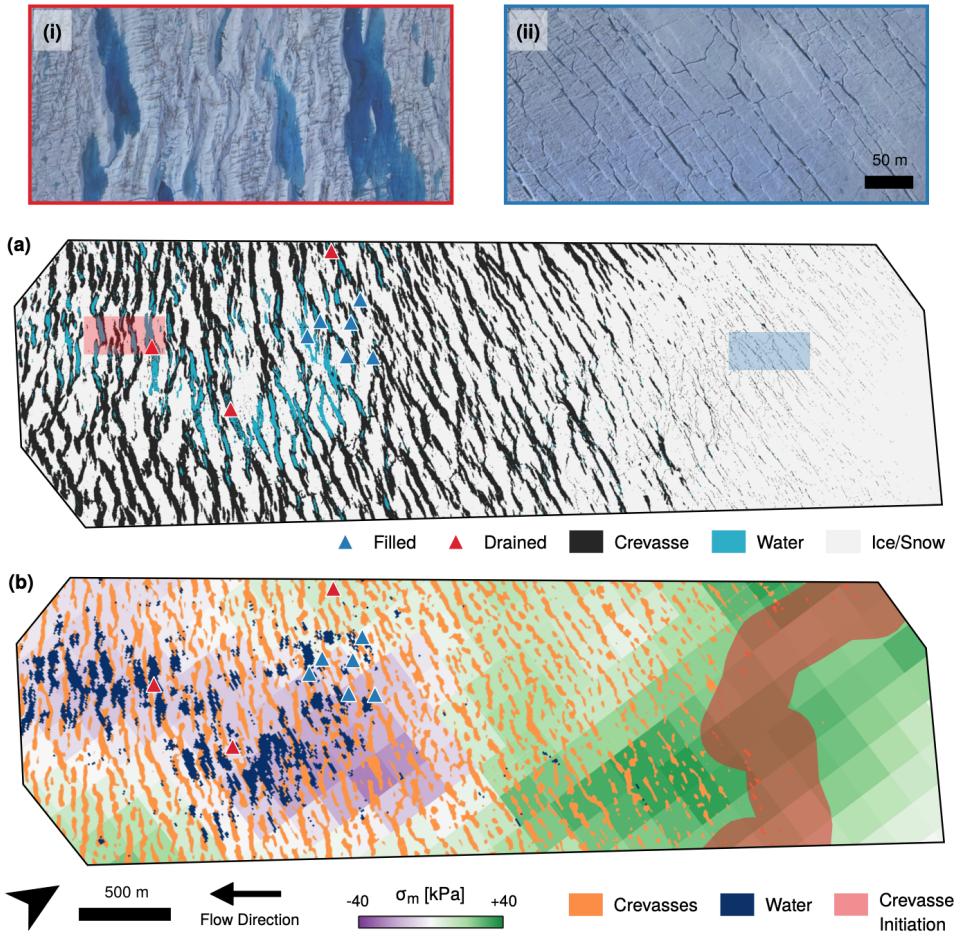

Figure 7. (a) Output of UAV random forest classification for 2018-07-08 survey, with insets (shaded in red and blue) showing (i) an area with large (widths 50-60 m) crevasses, and (ii) small (widths 2-3 m) crevasses. (b) Satellite-derived data for comparison, with meltwater extent from 2018.

crevasses fill with water when in a compressional mean stress regime, but also show that drainages of these ponded crevasses occur discreetly and rapidly.

Within the UAV-derived data, our observations do not indicate significant lateral meltwater routing. Where supraglacial streams routed water between ponded crevasses, they were easily identified in imagery (Figure S6a), but this was not common across the UAV ROI. When individual crevasses drained, observations of any consequential effects on the surrounding system was limited. For the two most prominent crevasse drainages (Figure 8), we identify the adjacent crevasses that also drained, either through visible supraglacial networks (marked 'S' in Figure 8), or without visible supraglacial connections, which we thus interpret to be connected englacially (marked 'E' in Figure 8). In the first case (Figure 8a), an overflowing crevasse system formed local supraglacial networks, and after one crevasse had drained, water levels across the entire network dropped (Figure 8b). However, only one adjacent crevasse drained without visible surface routing (Figure 8b). In the days following the drainage event, incised supraglacial channels formed between the previously overflowing system (Figure S6b–c). In the second drainage case, an individual crevasse drained without affecting water levels in the adjacent crevasses at all (Figure 8c–d). As such, in the ponded crevasse system within the UAV

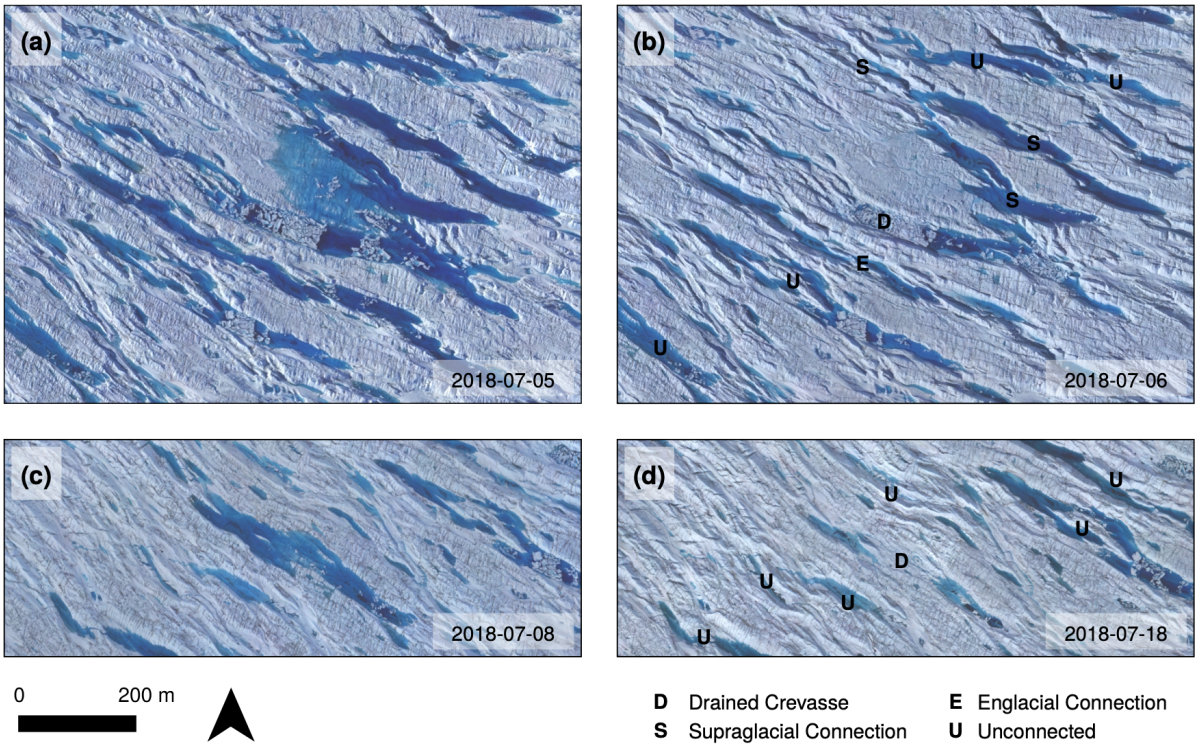

Figure 8. Examples of crevasse drainage (a) before and (b) after a crevasse drained that was supraglacially and/or englacially connected to adjacent crevasses; and (c) before and (d) after a crevasse drained where no connections were present. Interpretations are marked where crevasses underwent direct drainage (D), drained via a visible supraglacial connection to the draining crevasse (S), drained via inferred englacial connection to the draining crevasse (E), or remained unconnected to a draining system and did not drain (U).

ROI, we do not observe hydrological responses to drainage events that extend more than 1-2 crevasses (~100-200 m) from the initiating crevasse.

4 Discussion

4.1 Performance of satellite- and UAV-based classification methods

The object-based random forest classification of UAV data (Figure 7a) enabled the identification of crevasses and surface water with >95% accuracy (Figure S4; Table S2). Comparison of the UAV and satellite-derived surface classifications (Figure 7a cf. 7b) shows clear agreement in the distribution of surface features. The cutoff width below which crevasses are unable to be identified from ArcticDEM v3 data is ~10 m (~5 pixels). Although this cutoff means the satellite data do not identify the smallest crevasses (such as those in Figure 7ii), the resolvable size of a crevasse is approximately equal to the resolution of the Sentinel-2 bands used for NDWI calculation (10 m), allowing the two satellite-derived datasets to be compared directly. Despite the ArcticDEM mosaic being derived from multitemporal data (individual tiles across the satellite ROI range from 2009-2017), the distribution of crevasses is consistent with the 2018 UAV dataset (Figure 7a cf. 7b). This indicates that, regardless of the advection of individual

crevasses, interannual variation in crevasse field extent is minor across the time period in this study. We can therefore be confident that the ArcticDEM 2009-2017 crevasse distribution can be meaningfully compared to the Sentinel-2 2017-2019 surface water distribution. Sentinel-2- and UAV-derived surface water locations also agree consistently (Figure 7a cf. 7b), with individual ponded crevasses able to be co-located between the Sentinel-2 and UAV datasets. The Sentinel-2 data additionally identifies ponded crevasses that were not water-filled on the date of the UAV survey. In summary, the UAV data shows that we can be largely confident in our satellite-derived crevasse and water mapping at spatial scales ≥10 m. It is likely that the ArcticDEM-based crevasse mapping underestimated crevasse extent at higher elevations, as the optically-derived dataset will not be sensitive to snow-filled crevasses; however, false negative classifications do not affect the conclusions drawn from this dataset.

4.2 Spatial variability in crevasse hydrology

Across the ~2,700 km^2 study area, an average of 26% of the crevassed region (containing crevasses >10 m in width) exhibited visible ponding between 2017 and 2019. The inter-annual variation in ponded crevasse coverage was lowest in 2017 and highest in 2019, consistent with the lowest and highest reported ice-sheet-wide melt data (e.g. Tedesco and Fettweis, 2020) which identified 2019 as an exceptional melt year. This suggests that the extent of crevasse ponding is in part controlled by melt intensity, consistent with previous models conceptualising crevasses as linear reservoirs (Colgan *et al.,* 2011; McGrath *et al* 2011), i.e. as melt intensity increases beyond the capacity of crevasses to discharge water into the englacial system, more ponding will be observed at the surface. However, inter-annual melt intensity cannot explain the spatial distribution of observed ponding. Only a minority of crevasses are observed to pond, and the spatial distribution of these is consistent from year-to-year (Figure 3i-iii). These patterns occur on scales <1 km, smaller than any reasonable spatial boundary in melt intensity resulting from surface mass-balance drivers such as the vertical gradient in air temperature. This inference is supported by statistical tests that rejected the hypothesis that crevasse ponding was more prevalent at lower elevations within the ablation zone, where surface melt intensity is generally higher. These local-scale patterns of crevasse ponding are also stable in space regardless of ice velocity, suggesting that ponding incidence is not advected with individual crevasses. We therefore conclude that likely controls on the incidence of crevasse ponding are: (i) distinct from melt intensity; (ii) not associated with the properties of individual crevasses; and (iii) spatially variable on the order of 10^2 - 10^3 m.

4.3 Controls on crevasse hydrology

Previous studies have predicted the location of current and future supraglacial lakes on the Greenland Ice Sheet by identifying depressions in the surface topography that would capture supraglacial meltwater (e.g. Ignéczi *et al.,* 2016). This could be reasonably applied to crevasse ponding if meltwater could be routed, without obstruction, for long distances laterally along hydrological gradients across crevasse fields. This would result in localised crevasse ponding within surface depressions, forming a single surface lake if water supply exceeded open crevasse volume. However, our satellite observations suggest only a small fraction of crevassed area behaves in this way: only 9.7% of the ponded crevasse region is located within surface depressions (cf. 5.0% of all crevasses and 78.9% of the supraglacial lake area). This suggests that lateral supraglacial transport of water into topographic basins is not the principal cause of

crevasse ponding. Indeed, because ponding occurs across topographic highs (Figure 4), we infer that in ponded crevasse systems drainage into the wider supraglacial and/or englacial drainage system is being restricted. This inference is supported by our UAV repeat surveys, which show that hydrological connections between ponded crevasses - whether supraglacial or englacial - are rare and have limited spatial extent, often between only a few crevasses on the scale of 100-200 m (Figure 8b,d). Even where hydrological connections exist, they appear to form as a consequence, rather than a cause, of crevasse drainage (Figure S6b–c). If lateral meltwater flow is restricted, the drainage of water from ponded crevasse systems cannot, for the most part, be caused by water being routed into wider supraglacial networks (and from there to moulins, lakes, or the englacial system). This contrasts with previous studies, which often assume that lateral supraglacial drainage can occur unrestricted across crevasse fields (e.g. Poinar, 2015, Clason *et al.,* 2015).

In our satellite- and UAV-derived datasets, ponded crevasses are largely restricted to regions of compressive mean stress. This association may be explained by supraglacial and englacial drainage remaining open and well-connected across crevasse fields in areas characterized by extensional mean stress regimes. This is consistent with the view of crevasse systems on temperate valley glaciers as hydraulically connected, albeit inefficiently, to englacial and/or subglacial drainage systems through a linked network of fractures (Fountain *et al.,* 2005), and supported by radar observations at Sermeq Kujalleq (Store Glacier), where englacial meltwater storage in crevasse-damaged ice has been inferred down to a depth of 48 m (Kendrick *et al.,* 2018). In these systems, meltwater availability rarely exceeds drainage rate, explaining the limited crevasse ponding observed in such extensional regions. In contrast, we suggest that in compressive regimes, englacial connections undergo what Irvine-Fynn *et al.* (2011) described as 'pinch-off', whereby crevasse closure by ice creep hydraulically isolates crevasse systems from the wider supraglacial and englacial drainage system, resulting in subsequent ponding. This hypothesis is supported by our UAV data, which show that englacial connections between crevasses in ponded regions are limited in prevalence and extent. While a compressive mean stress regime appears to be a necessary condition for crevasse ponding, not all crevasses located within such regimes are water-filled (Figure 6). This may be because the englacial system does not always close entirely: we note that, at the UAV ROI, the upstream ~400 m of the compressive stress field does not exhibit ponding (Figure 7b), perhaps indicating a delay before the crevasse system is fully isolated. As the velocity at the UAV ROI is ~650 m a^{-1}, this would indicate a closure time of ~7 months to isolate the system.

4.4 Inferred drainage mechanisms and potential implications

4.4.1 Rapid drainage of ponded crevasses

Given that we found little direct evidence for hydrological connections between crevasses in ponded regimes (Section 4.2), we consider full-depth hydrofracture and drainage to the subglacial environment to be a likely mechanism by which ponded crevasses drain (Weertman, 1973; Boon & Sharp, 2003; van der Veen, 2007; Krawczynski *et al.,* 2009). This would be consistent with the rapid and heterogenous drainages observed in UAV data. Analogous to supraglacial lake drainages via rapid hydrofracture (Das *et al.,* 2008; Doyle *et al.,* 2013; Stevens *et al.,* 2015; Chudley *et al.,* 2019b), rapid crevasse drainage events are expected to deliver distinct, isolated pulses of meltwater to the bed. The full dynamic consequences of such events

525 are explored in detail elsewhere (e.g. Nienow *et al.,* 2017), but it is apparent that meltwater
526 inputs to the bed that are rapid (Schoof, 2010) and spatially discrete (Banwell *et al.,* 2016) can
527 influence ice dynamics. For example, rapidly draining crevasse systems at the shear margin of
528 Jakobshavn Isbrae have been shown to deliver meltwater to the bed at sufficient rates and
529 volumes to overwhelm the capacity of the subglacial system (Lampkin *et al.,* 2013), increasing
530 ice mass flux across the shear margin and enhancing glacier discharge (Cavanagh *et al.,* 2017;
531 Lampkin *et al.,* 2018).

532 There are, however, several features of rapid crevasse drainages that are distinct from more
533 widely studied lake drainage events. After hydrofracture, ongoing meltwater delivery via the
534 newly open moulin represents an important hydrological component of lake drainages (Koziol *et*
535 *al.,* 2017; Hoffman *et al.,* 2018). In contrast, the smaller catchments of individual crevasses
536 means that this effect is likely less important following crevasse drainage (although crevasses are
537 more numerous than lakes). Further, unlike lakes, it appears to be relatively common that
538 crevasse systems can drain multiple times through a single ablation season (Cavanagh *et al.,*
539 2017). However, the net effect of this on ice dynamics has yet to be identified. Additionally,
540 crevasses that remain ponded and then refreeze at the end of the season will release latent heat
541 and facilitate ice warming (Lüthi *et al.,* 2015) at depths of up to hundreds of metres (Hubbard *et*
542 *al.,* in press).

543 *4.4.2 Slow drainage of dry crevasses*

544 Approximately 74% of crevasse fields display no evidence of ponded meltwater (which we refer
545 to as 'dry' crevasses), despite there being no difference in local meltwater availability compared
546 to adjacent ponded regions. Since meltwater is inevitably also routed into these dry crevasses, we
547 suggest that this water is accommodated by the wider supraglacial and englacial hydrological
548 system, stored and/or routed through pre-existing englacial pathways (e.g. Figure S7) or linked
549 fracture networks (Fountain *et al.,* 2005; Kendrick *et al.,* 2018), all of which are maintained by
550 an extensional stress regime. Since no ponding is observed in these regions, the condition for
551 hydrofracture is restricted, meaning that these crevasses are unlikely to route meltwater directly
552 to the bed. Instead, we suggest that this laterally routed meltwater must eventually intersect pre-
553 existing moulins (Catania and Neumann, 2010), terminate at supraglacial lakes, remain as a
554 liquid reservoir (Kendrick *et al.,* 2018), or freeze during the winter season.

555 We conceptualise that, due to low rates of lateral meltwater transport, drainage in dry crevasse
556 systems has a long total transit time to the bed. Such slow, continuous crevasse drainage has
557 previously been applied in crevasse hydrological models at the Greenland Ice Sheet by Colgan *et*
558 *al.* (2011) and McGrath *et al.* (2011). Colgan *et al.* (2011) suggested crevasse surface-to-bed
559 delivery rates may be 200-fold slower than moulins (~12 hours for a 0.1 m wide crevasse cf. ~1
560 hour for a 1 m^2 moulin), whilst McGrath *et al.* (2011) suggested that crevasses may slow
561 englacial drainage to such an extent that a diurnal cycle of meltwater input can be damped to a
562 quasi-steady state discharge on the timescale of hours-days. This slow and sustained delivery of
563 meltwater through crevasses to the glacier bed would be less likely to overwhelm temporarily the
564 transmission capacity of the subglacial drainage system. Therefore, both studies argue that
565 regions of the bed subject to this style of meltwater delivery are less likely to exhibit
566 ephemerally-enhanced basal sliding compared to regions experiencing episodic, efficient
567 meltwater pulses (as in Section 4.4.1). Additionally, this slower englacial drainage style

associated with crevasses may have distinct thermal consequences. It has been argued that slow meltwater delivery through crevasses would deliver latent heat that results in more cryo-hydrologic warming relative to regions fed by discrete moulins (Colgan *et al.,* 2011) because densely packed and slow hydrological pathways increase the volume of ice warmed by the latent heat release of englacial freezing relative to efficient drainage pathways (Phillips *et al.,* 2010; Lüthi *et al.,* 2015). As full-depth hydrofracture is likely restricted in dry crevasse systems, drainage in these regions may deliver less latent heat into depths on the order of hundreds of metres compared to ponded crevasses, where propagation is facilitated by hydrofracture (e.g. Poinar, 2015).

4.5 Implications for hydrological routing models

In the past, regional models of ice sheet hydrology and dynamics have often failed to include crevasse drainage, instead focusing exclusively on supraglacial lake drainage (e.g. Arnold *et al.,* 2014; Banwell *et al.,* 2013, 2016). Recent regional hydrological models have begun to include crevasse drainage in simple ways. For example, Clason *et al.* (2015) incorporated crevasse drainage, but considered it similarly to supraglacial lake drainage. These authors identified crevassed regions based on a σ_v threshold, which were then allowed to fill and hydrofracture according to a LEFM model (van der Veen, 2007). After full-depth hydrofracture and drainage, a moulin was formed that continued to drain any further meltwater continuously to the bed. More recently, Koziol *et al.* (2017) allowed crevasses to continuously drain, with meltwater produced at the surface of crevasse fields (again identified according to a σ_v threshold) drained immediately to the bed without requiring hydrofracture. These behaviours, reflecting a paucity of observations available at the time, were assumed to be spatially uniform. The observational results we present herein highlight ways, summarized below, in which future studies may be able to account further for a wide diversity of crevasse hydrology while keeping inputs and classifications as simple as possible.

Our first recommendation is to avoid using simple stress thresholds or zero stress models to predict crevasse presence in surface routing models. Several models that incorporate crevasse drainage have used a von Mises yield criterion (following Vaughan, 1993) to estimate the location of crevasses for water routing (Clason *et al.,* 2015; Koziol *et al.,* 2017), as well as to approximate tensile stress in crevasse hydrofracture (Clason *et al.,* 2015, Morlighem *et al.,* 2016). However, our data indicate that von Mises yield stress, σ_v, is not the most appropriate predictor of crevasse incidence and hydrology. Indeed, our analysis indicates that crevasses exist across a range of σ_v values, both above and below the yield threshold prescribed following the method of Vaughan (1993) (Figure 5b). Furthermore, our data indicate that even broad regions of ice failure are not predicted accurately by a von Mises yield criterion (Figure 5c), with initiating crevasses existing predominantly: (i) below the 76 kPa threshold prescribed following Vaughan (1993), and (ii) in regions of positive mean stress. This is unsurprising considering that the compressive strength of ice greatly exceeds its tensile strength, a factor that von Mises stress is insensitive to. As such, we do not recommend a von Mises yield criterion as a suitable threshold for identifying regions of crevasse incidence. While alternative measures, such as the first principal (Benn *et al.,* 2007) or longitudinal (Harper *et al.,* 1998) stress, may be more appropriate for predicting brittle ice failure, they are unlikely to also be a useful threshold for predicting crevasse field distribution (Colgan *et al.,* 2016), as crevasses advecting into unviable stress regimes take time to adjust to the new equilibrium (Mottram and Benn, 2009). For studies of

contemporary crevasse fields, we instead recommend the use of direct observations as the simplest and most practical way to map crevasse locations. Herein, we present a simple method to achieve this based on the analysis of high-resolution DEMs, but other studies have adopted alternative methods such as using convolutional neural networks to classify optical imagery (Lai *et al.,* 2020). However, using satellite-derived data comes with weaknesses, such as being unable to identify crevasses under snow cover or below the spatial resolution of the input data. The clustering of incipient crevasses in extensional mean stress regimes (Figure 5c) suggests that models could properly map crevasses from surface stresses if a more suitable stress threshold were to be identified and subsequent advection and closure could be accounted for (e.g. Albrecht and Levermann, 2014).

Our second recommendation is to begin accounting for the diverse representations of crevasse drainage. Our data suggests that the delivery of supraglacial meltwater to the glacier bed through crevasses falls into a spectrum of behaviour, ranging from episodic rapid drainage via full-depth hydrofracture (Section 4.4.1) to slow and continuous englacial drainage (Section 4.4.2). At the coarsest scale, it may be desirable to implement a binary system to account for the end-members of this spectrum. Our data suggest that the mean surface-parallel stress is a useful way of segregating crevasse hydrological behaviour, with crevasses in compressive regimes being hydrologically isolated and exhibiting episodic rapid drainage. In contrast, crevasses in extensional regimes are hydraulically connected, exhibiting continuous drainage into the wider supraglacial and englacal system. Thus, in compressive regimes, drainage could be modelled as episodic rapid hydrofracture following Clason *et al.* (2015), while also restricting the lateral flow of meltwater between grid cells. In extensional regimes, meltwater could be routed laterally to the nearest moulin or supraglacial lake. Simple thresholding such as this could be used in regional hydrological models to investigate the seasonal and long-term effects of spatial heterogeneity in crevasse hydrology on subglacial hydrology and ice sheet dynamics (see, for example, Poinar *et al.,* 2019).

5 Conclusions

Previous work on Greenland's surface hydrology has assumed that water flow through crevasses, if considered at all, is spatially homogeneous and can be predicted using simple physical thresholds. Our analysis of regional satellite data and local UAV surveys has demonstrated that crevasses instead exhibit spatially variable but inter-annually persistent hydrology across a ~2,700 km^2 marine-terminating sector of the western GrIS. Only 26% of crevasses are observed to pond, which we infer to result from the hydraulic isolation of crevasse systems in areas of compressive mean surface-parallel stress. Through UAV surveys, these ponded crevasses were shown to drain rapidly and episodically, likely through full-depth hydrofracture. The remaining 74% of crevasses stay dry throughout the observational period, which we infer to be due to water draining into the wider englacial and supraglacial system, connected through linked fracture networks that are actively maintained in extensional stress regimes. Our findings indicate that controls on crevasse ponding are distinct from better-studied processes, such as supraglacial lake formation and crevasse opening, that are often used to represent the mechanics of crevasse hydrology in surface routing models. This highlights the need for a better implementation of crevasse hydrology in surface routing models, particularly as early implementations show that crevasses can act as pathways for nearly half of all meltwater (Koziol *et al.,* 2017). Our observations indicate that some form of simple stress threshold may still be suitable to drive

parameterisations in regional-scale models of meltwater drainage. However, further observations are necessary to improve our process-based understanding of crevasse hydrology, including *in-situ* observations of crevasse-scale mechanics and ice-sheet-scale satellite observations of spatio-temporal variability. Understanding the full spectrum of variability in crevasse hydrology is not only essential to be able to model the Greenland Ice Sheet's thermodynamic response to increasing surface runoff in the 21st century, but has wider implications across other cryospheric contexts, such as ice shelf hydrology and breakup (e.g. Lai *et al.,* 2020).

Acknowledgments and Data

This research was funded by the European Research Council as part of the RESPONDER project under the European Union's Horizon 2020 research and innovation program (Grant 683043). TRC and RL were supported by a Natural Environment Research Council Doctoral Training Partnership Studentship (Grant NE/L002507/1). We are very grateful to Ann Andreasen and the Uummannaq Polar Institute for their kind hospitality, to Sean Peters for his assistance with UAV launches, and to Neil Arnold for useful methodological discussions.

MEaSUREs annual velocity mosaics are available from the National Snow and Ice Data Centre (https://doi.org/10.5067/OBXCG75U7540). Sentinel-2 and ArcticDEM v3 data were made available for processing via Google Earth Engine. Upon publication, data products will be made available via the UK Polar Data Centre (UK PDC).

The authors declare no conflicts of interest.

References

Achanta, R., & Süsstrunk, S. (2017). Superpixels and Polygons Using Simple Non-iterative Clustering. In *2017 IEEE Conference on Computer Vision and Pattern Recognition (CVPR)* (pp. 4895–4904). https://doi.org/10.1109/CVPR.2017.520

Alley, R. B., Dupont, T. K., Parizek, B. R., & Anandakrishnan, S. (2005). Access of surface meltwater to beds of sub-freezing glaciers: preliminary insights. *Annals of Glaciology*, *40*, 8–14. https://doi.org/10.3189/172756405781813483

Arnold, N. S., Banwell, A. F., & Willis, I. C. (2014). High-resolution modelling of the seasonal evolution of surface water storage on the Greenland Ice Sheet. *The Cryosphere*, *8*(4), 1149–1160. https://doi.org/10.5194/tc-8-1149-2014

Banwell, A., Hewitt, I., Willis, I., & Arnold, N. (2016). Moulin density controls drainage development beneath the Greenland ice sheet. *Journal of Geophysical Research: Earth Surface*, 2015JF003801. https://doi.org/10.1002/2015JF003801

Banwell, A. F., Willis, I. C., & Arnold, N. S. (2013). Modeling subglacial water routing at Paakitsoq, W Greenland. *Journal of Geophysical Research: Earth Surface*, *118*(3), 1282–1295. https://doi.org/10.1002/jgrf.20093

Benn, D. I., Warren, C. R., & Mottram, R. H. (2007). Calving processes and the dynamics of calving glaciers. Earth-Science Reviews, 82(3), 143–179. https://doi.org/10.1016/j.earscirev.2007.02.002

Benn, D. I., Åström, J., Zwinger, T., Todd, J., Nick, F. M., Cook, S., *et al.* (2017). Melt-under-cutting and buoyancy-driven calving from tidewater glaciers: new insights from discrete element and continuum model simulations. *Journal of Glaciology*, *63*(240), 691–702. https://doi.org/10.1017/jog.2017.41

Blaschke, T. (2010). Object based image analysis for remote sensing. *ISPRS Journal of Photogrammetry and Remote Sensing*, *65*(1), 2–16. https://doi.org/10.1016/j.isprsjprs.2009.06.004

Boon, S., & Sharp, M. (2003). The role of hydrologically-driven ice fracture in drainage system evolution on an Arctic glacier. *Geophysical Research Letters*, *30*(18). https://doi.org/10.1029/2003GL018034

Cavanagh, J. P., Lampkin, D. J., & Moon, T. (2017). Seasonal Variability in Regional Ice Flow Due to Meltwater Injection Into the Shear Margins of Jakobshavn Isbræ. *Journal of Geophysical Research: Earth Surface*, *122*(12), 2488–2505. https://doi.org/10.1002/2016JF004187

Christoffersen, P., Bougamont, M., Hubbard, A., Doyle, S. H., Grigsby, S., & Pettersson, R. (2018). Cascading lake drainage on the Greenland Ice Sheet triggered by tensile shock and fracture. *Nature Communications*, *9*(1), 1064. https://doi.org/10.1038/s41467-018-03420-8

Chudley, T. R., Christoffersen, P., Doyle, S. H., Abellan, A., & Snooke, N. (2019a). High-accuracy UAV photogrammetry of ice sheet dynamics with no ground control. *The Cryosphere*, *13*(3), 955–968. https://doi.org/10.5194/tc-13-955-2019

Chudley, T. R., Christoffersen, P., Doyle, S. H., Bougamont, M., Schoonman, C. M., Hubbard, B., & James, M. R. (2019b). Supraglacial lake drainage at a fast-flowing Greenlandic outlet glacier. *Proceedings of the National Academy of Sciences*. https://doi.org/10.1073/pnas.1913685116

Clason, C. C., Mair, D. W. F., Nienow, P. W., Bartholomew, I. D., Sole, A., Palmer, S., & Schwanghart, W. (2015). Modelling the transfer of supraglacial meltwater to the bed of Leverett Glacier, Southwest Greenland. *The Cryosphere*, *9*(1), 123–138. https://doi.org/10.5194/tc-9-123-2015

Colgan, W., Steffen, K., McLamb, W. S., Abdalati, W., Rajaram, H., Motyka, R., *et al.* (2011). An increase in crevasse extent, West Greenland: Hydrologic implications. *Geophysical Research Letters*, *38*(18). https://doi.org/10.1029/2011GL048491

Colgan, W., Rajaram, H., Abdalati, W., McCutchan, C., Mottram, R., Moussavi, M. S., & Grigsby, S. (2016). Glacier crevasses: Observations, models, and mass balance implications. *Reviews of Geophysics*, *54*(1), 119–161. https://doi.org/10.1002/2015RG000504

Cuffey, K. M., & Paterson, W. S. B. (2010). *The physics of glaciers*. Academic Press.

Das, S. B., Joughin, I., Behn, M. D., Howat, I. M., King, M. A., Lizarralde, D., & Bhatia, M. P. (2008). Fracture Propagation to the Base of the Greenland Ice Sheet During Supraglacial Lake Drainage. *Science*, *320*(5877), 778–781. https://doi.org/10.1126/science.1153360

Dell, R., Carr, R., Phillips, E., & Russell, A. J. (2019). Response of glacier flow and structure to proglacial lake development and climate at Fjallsjökull, south-east Iceland. *Journal of Glaciology*, 1–16. https://doi.org/10.1017/jog.2019.18

Doyle, S. H., Hubbard, A. L., Dow, C. F., Jones, G. A., Fitzpatrick, A., Gusmeroli, A., *et al.* (2013). Ice tectonic deformation during the rapid in situ drainage of a supraglacial lake on the Greenland Ice Sheet. *The Cryosphere*, *7*(1), 129–140. https://doi.org/10.5194/tc-7-129-2013

Everett, A., Murray, T., Selmes, N., Rutt, I. C., Luckman, A., James, T. D., *et al.* (2016). Annual down-glacier drainage of lakes and water-filled crevasses at Helheim Glacier, southeast Greenland. *Journal of Geophysical Research: Earth Surface*, *121*(10), 1819–1833. https://doi.org/10.1002/2016JF003831

Florinsky, I. V., & Bliakharskii, D. P. (2019). Detection of crevasses by geomorphometric treatment of data from unmanned aerial surveys. *Remote Sensing Letters*, *10*(4), 323–332. https://doi.org/10.1080/2150704X.2018.1552809

Fountain, A. G., Jacobel, R. W., Schlichting, R., & Jansson, P. (2005). Fractures as the main pathways of water flow in temperate glaciers. *Nature*, *433*(7026), 618–621. https://doi.org/10.1038/nature03296

Glen, J. W. (1955). The creep of polycrystalline ice. *Proceedings of the Royal Society of London. Series A. Mathematical and Physical Sciences*, *228*(1175), 519–538. https://doi.org/10.1098/rspa.1955.0066

Gorelick, N., Hancher, M., Dixon, M., Ilyushchenko, S., Thau, D., & Moore, R. (2017). Google Earth Engine: Planetary-scale geospatial analysis for everyone. *Remote Sensing of Environment*, *202*, 18–27. https://doi.org/10.1016/j.rse.2017.06.031

Hambrey, M. J., & Müller, F. (1978). Structures and ice deformation in the white glacier, Axel Heiberg Island, Northwest Territories, Canada. *Journal of Glaciology*, *20*(82), 41–66. https://doi.org/10.3189/S0022143000021213

Harper, J. T., Humphrey, N. F., & Pfeffer, W. T. (1998). Crevasse patterns and the strain-rate tensor: a high-resolution comparison. *Journal of Glaciology*, *44*(146), 68–76. https://doi.org/10.3189/S0022143000002367

Hoffman, M. J., Perego, M., Andrews, L. C., Price, S. F., Neumann, T. A., Johnson, J. V., *et al.* (2018). Widespread Moulin Formation During Supraglacial Lake Drainages in Greenland. *Geophysical Research Letters*, 2017GL075659. https://doi.org/10.1002/2017GL075659

Howat, I. M., Negrete, A., & Smith, B. E. (2014). The Greenland Ice Mapping Project (GIMP) land classification and surface elevation data sets. *The Cryosphere*, *8*(4), 1509–1518. https://doi.org/10.5194/tc-8-1509-2014

Hubbard, B., Christoffersen, P., Doyle, S. H., Chudley, T. R., Schoonman, C. M., Law, R., & Bougamont, M. (in press). Borehole-based characterization of deep crevasses at a Greenlandic outlet glacier. *AGU Advances*.

Ignéczi, Á., Sole, A. J., Livingstone, S. J., Leeson, A. A., Fettweis, X., Selmes, N., *et al.* (2016). Northeast sector of the Greenland Ice Sheet to undergo the greatest inland expansion of supraglacial lakes during the 21st century. *Geophysical Research Letters, 43*(18), 9729–9738. https://doi.org/10.1002/2016GL070338

Irvine-Fynn, T. D., Hodson, A. J., Moorman, B. J., Vatne, G., & Hubbard, A. L. (2011). Polythermal glacier hydrology: A review. *Reviews of Geophysics*, *49*(4). https://doi.org/10.1029/2010RG000350

Jones, C., Ryan, J., Holt, T., & Hubbard, A. (2018). Structural glaciology of Isunguata Sermia, West Greenland. *Journal of Maps*, *14*(2), 517–527. https://doi.org/10.1080/17445647.2018.1507952

Joughin, I., Smith, B. E., Howat, I. M., Scambos, T., & Moon, T. (2010). Greenland flow variability from ice-sheet-wide velocity mapping. *Journal of Glaciology*, *56*(197), 415–430. https://doi.org/10.3189/002214310792447734

Kodde, M. P., Pfeifer, N., Gorte, B. G. H., Geist, T., & Höfle, B. (2007). Automatic glacier surface analysis from airborne laser scanning. *International Archives of the Photogrammetry, Remote Sensing and Spatial Information Sciences*, *36*(3), 221–226.

Koziol, C., Arnold, N., Pope, A., & Colgan, W. (2017). Quantifying supraglacial meltwater pathways in the Paakitsoq region, West Greenland. *Journal of Glaciology*, 1–13. https://doi.org/10.1017/jog.2017.5

Koziol, C. P., & Arnold, N. (2018). Modelling seasonal meltwater forcing of the velocity of the Greenland Ice Sheet. https://doi.org/10.5194/tc-12-971-2018

Kraaijenbrink, P. D. A., Shea, J. M., Pellicciotti, F., Jong, S. M. de, & Immerzeel, W. W. (2016). Object-based analysis of unmanned aerial vehicle imagery to map and characterise surface features on a debris-covered glacier. *Remote Sensing of Environment*, *186*, 581–595. https://doi.org/10.1016/j.rse.2016.09.013

Kraaijenbrink, Philip Derk Andreas, Shea, J. M., Litt, M., Steiner, J. F., Treichler, D., Koch, I., & Immerzeel, W. W. (2018). Mapping Surface Temperatures on a Debris-Covered Glacier with an Unmanned Aerial Vehicle. *Frontiers in Earth Science*, *6*. https://doi.org/10.3389/feart.2018.00064

Krawczynski, M. J., Behn, M. D., Das, S. B., & Joughin, I. (2009). Constraints on the lake volume required for hydro-fracture through ice sheets. *Geophysical Research Letters*, *36*(10). https://doi.org/10.1029/2008GL036765

Lampkin, D. J., Amador, N., Parizek, B. R., Farness, K., & Jezek, K. (2013). Drainage from water-filled crevasses along the margins of Jakobshavn Isbræ: A potential catalyst for catchment expansion. *Journal of Geophysical Research: Earth Surface*, *118*(2), 795–813. https://doi.org/10.1002/jgrf.20039

Lampkin, Derrick J., Parizek, B., Larour, E. Y., Seroussi, H., Joseph, C., & Cavanagh, J. P. (2018). Toward Improved Understanding of Changes in Greenland Outlet Glacier Shear Margin Dynamics in a Warming Climate. *Frontiers in Earth Science*, *6*. https://doi.org/10.3389/feart.2018.00156

Law, R., Christoffersen, P., Hubbard, B., Doyle, S. H., Chudley, T. R., Schoonman, C. M., *et al.* (in press). Thermodynamics of a fast-moving Greenlandic outlet glacier revealed by fiber-optic distributed temperature sensing. *Science Advances*.

Lüthi, M. P., Ryser, C., Andrews, L. C., Catania, G. A., Funk, M., & Hawley, R. L. (2015). Heat sources within the Greenland Ice Sheet: dissipation, temperate paleo-firn and cryo-hydrologic warming. *The Cryosphere*. https://doi.org/10.5194/tc-9-245-2015

McGrath, D., Colgan, W., Steffen, K., Lauffenburger, P., & Balog, J. (2011). Assessing the summer water budget of a moulin basin in the Sermeq Avannarleq ablation region, Greenland ice sheet. *Journal of Glaciology*, *57*(205), 954–964. https://doi.org/10.3189/002214311798043735

Mottram, R. H., & Benn, D. I. (2009). Testing crevasse-depth models: a field study at Breiðamerkurjökull, Iceland. *Journal of Glaciology*, *55*(192), 746–752. https://doi.org/10.3189/002214309789470905

Nienow, P. W., Sole, A. J., Slater, D. A., & Cowton, T. R. (2017). Recent Advances in Our Understanding of the Role of Meltwater in the Greenland Ice Sheet System. *Current Climate Change Reports*, 1–15. https://doi.org/10.1007/s40641-017-0083-9

Nye, J. F. (1957). The distribution of stress and velocity in glaciers and ice-sheets. *Proceedings of the Royal Society of London. Series A. Mathematical and Physical Sciences*, *239*(1216), 113–133. https://doi.org/10.1098/rspa.1957.0026

Phillips, E., Finlayson, A., & Jones, L. (2013). Fracturing, block faulting, and moulin development associated with progressive collapse and retreat of a maritime glacier: Falljökull, SE Iceland. *Journal of Geophysical Research: Earth Surface*, *118*(3), 1545–1561. https://doi.org/10.1002/jgrf.20116

Phillips, T., Rajaram, H., & Steffen, K. (2010). Cryo-hydrologic warming: A potential mechanism for rapid thermal response of ice sheets. *Geophysical Research Letters*, *37*(20). Retrieved from http://onlinelibrary.wiley.com/doi/10.1029/2010GL044397/full

Poinar, K. (2015). *The influence of meltwater on the thermal structure and flow of the Greenland Ice Sheet* (Thesis). Retrieved from https://digital.lib.washington.edu:443/researchworks/handle/1773/35062

Poinar, K., & Andrews, L. C. (2021). Challenges in predicting Greenland supraglacial lake drainages at the regional scale. *The Cryosphere*, *15*(3), 1455–1483. https://doi.org/10.5194/tc-15-1455-2021

Poinar, K., Joughin, I., Das, S. B., Behn, M. D., Lenaerts, J. T. M., & van den Broeke, M. R. (2015). Limits to future expansion of surface-melt-enhanced ice flow into the interior of western Greenland. *Geophysical Research Letters*, *42*(6), 2015GL063192. https://doi.org/10.1002/2015GL063192

Poinar, K., Dow, C. F., & Andrews, L. C. (2019). Long-Term Support of an Active Subglacial Hydrologic System in Southeast Greenland by Firn Aquifers. *Geophysical Research Letters*, *46*(9), 4772–4781. https://doi.org/10.1029/2019GL082786

Pope, A. (2016). Reproducibly estimating and evaluating supraglacial lake depth with Landsat 8 and other multispectral sensors. *Earth and Space Science*, *3*(4), 176–188. https://doi.org/10.1002/2015EA000125

Porter, C., Morin, P., Howat, I., Noh, M.-J., Bates, B., Peterman, K., *et al.* (2018). ArcticDEM. Harvard Dataverse. Retrieved from 10.7910/DVN/OHHUKH

Ryan, J. C., Hubbard, A. L., Box, J. E., Todd, J., Christoffersen, P., Carr, J. R., *et al.* (2015). UAV photogrammetry and structure from motion to assess calving dynamics at Store Glacier, a large outlet draining the Greenland ice sheet. *The Cryosphere*, *9*(1), 1–11. https://doi.org/10.5194/tc-9-1-2015

Ryan, J. C., Hubbard, A., Stibal, M., Irvine-Fynn, T. D., Cook, J., Smith, L. C., *et al.* (2018). Dark zone of the Greenland Ice Sheet controlled by distributed biologically-active impurities. *Nature Communications*, *9*(1), 1065. https://doi.org/10.1038/s41467-018-03353-2

Schoof, C. (2010). Ice-sheet acceleration driven by melt supply variability. *Nature*, *468*(7325), 803–806. https://doi.org/10.1038/nature09618

Stevens, L. A., Behn, M. D., McGuire, J. J., Das, S. B., Joughin, I., Herring, T., *et al. (*2015). Greenland supraglacial lake drainages triggered by hydrologically induced basal slip. *Nature*, *522*(7554), 73–76. https://doi.org/10.1038/nature14480

Tedesco, M., & Fettweis, X. (2020). Unprecedented atmospheric conditions (1948–2019) drive the 2019 exceptional melting season over the Greenland ice sheet. *The Cryosphere*, *14*(4), 1209–1223. https://doi.org/10.5194/tc-14-1209-2020

Todd, J., Christoffersen, P., Zwinger, T., R\aaback, P., & Benn, D. I. (2019). Sensitivity of a calving glacier to ice—ocean interactions under climate change: new insights from a 3-D full-Stokes model. *The Cryosphere*. https://doi.org/10.5194/tc-13-1681-2019

Vaughan, D. G. (1993). Relating the occurrence of crevasses to surface strain rates. *Journal of Glaciology*, *39*(132), 255–266. https://doi.org/10.3189/S0022143000015926

van der Veen, C. J. (1998). Fracture mechanics approach to penetration of surface crevasses on glaciers. *Cold Regions Science and Technology*, *27*(1), 31–47. https://doi.org/10.1016/S0165-232X(97)00022-0

van der Veen, C. J. (1999). Crevasses on glaciers. *Polar Geography*, *23*(3), 213–245. https://doi.org/10.1080/10889379909377677

van der Veen, C. J. (2007). Fracture propagation as means of rapidly transferring surface meltwater to the base of glaciers. *Geophysical Research Letters*, *34*(1). https://doi.org/10.1029/2006GL028385

Weertman, J. (1973). Can a water-filled crevasse reach the bottom surface of a glacier. *IASH Publ*, *95*, 139–145.

Williamson, A. G., Banwell, A. F., Willis, I. C., & Arnold, N. S. (2018a). Dual-satellite (Sentinel-2 and Landsat 8) remote sensing of supraglacial lakes in Greenland. *The Cryosphere*, *12*(9), 3045–3065. https://doi.org/10.5194/tc-12-3045-2018

Williamson, A. G., Willis, I. C., Arnold, N. S., & Banwell, A. F. (2018b). Controls on rapid supraglacial lake drainage in West Greenland: an Exploratory Data Analysis approach. *Journal of Glaciology*, 1–19. https://doi.org/10.1017/jog.2018.8